nature portfolio

https://doi.org/10.1038/s41586-024-07831-0

Supplementary information

Highly variable magmatic accretion at the ultraslow-spreading Gakkel Ridge

In the format provided by the authors and unedited

Highly variable magmatic accretion at the ultraslow-spreading Gakkel Ridge

Tao Zhang[1], Jiabiao Li[1*], Xiongwei Niu[1], Weiwei Ding[1], Yinxia Fang[1], Jian Lin[2,3], Yejian Wang[1], Caicai Zha[3], Pingchuan Tan[1], Fansheng Kong[1], Jie Chen[4], Xiaodong Wei[1], Jianggu Lu[1], Jérôme Dyment[4], Jason P. Morgan[2]

[1]Key Laboratory of Submarine Geosciences, Second Institute of Oceanography, MNR, Hangzhou 310012, China.

[2]Advanced Institute for Ocean Research, Department of Ocean Science and Engineering, Southern University of Science and Technology, Shenzhen 518055, China.

[3]Key Laboratory of Ocean and Marginal Sea Geology, South China Sea Institute of Oceanology, Innovation Academy of South China Sea Ecology and Environmental Engineering, Chinese Academy of Sciences, Guangzhou 511458, China.

[4]Université Paris Cité, Institut de physique du globe de Paris, CNRS, Paris, F-75005, France.

*Corresponding author. Email: jbli@sio.org.cn

Supplementary information

This file contains Supplementary Figures 1–7 and Supplementary Tables 1–4.

Supplementary figures

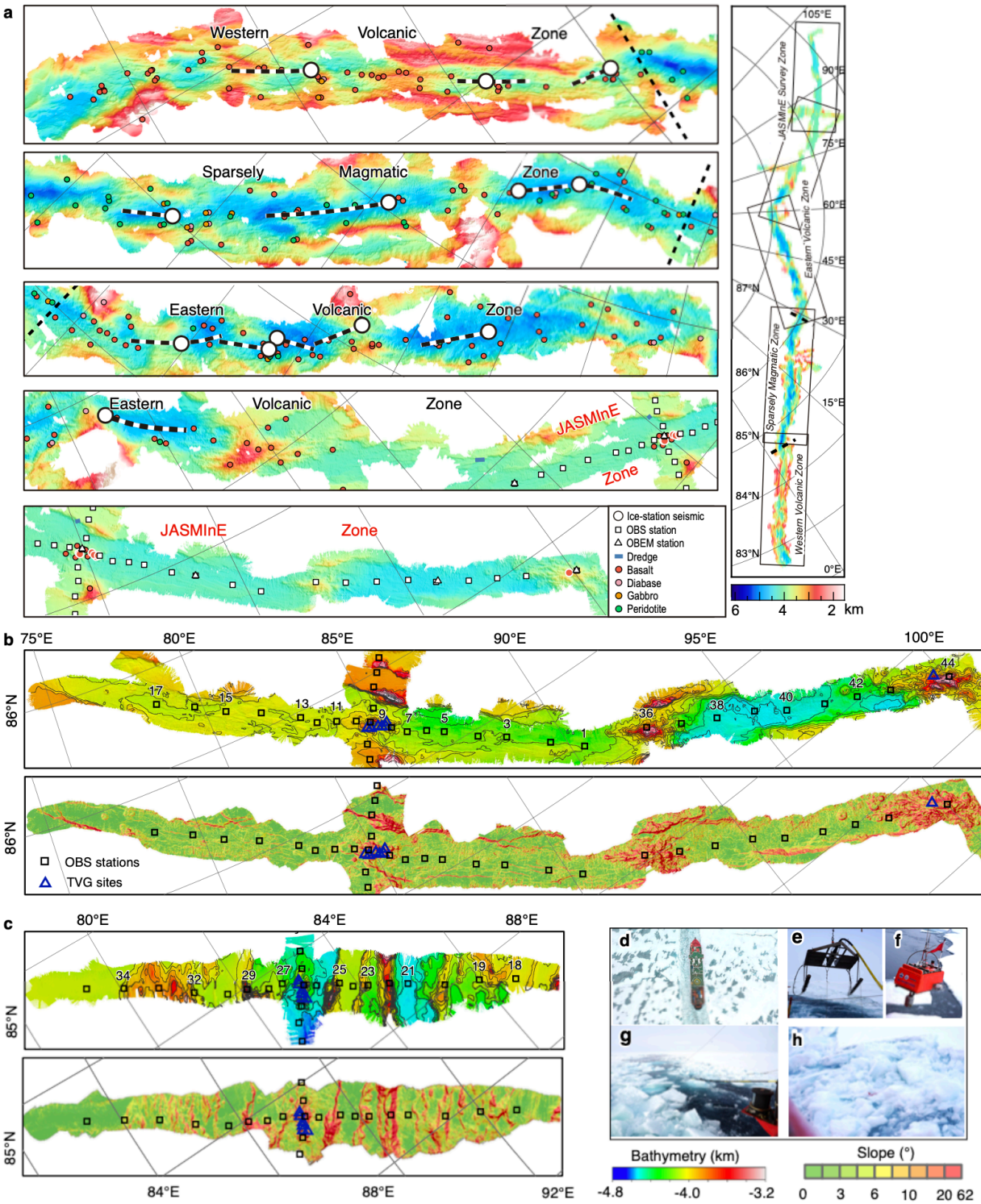

Supplementary Fig. 1 | Layout of seismic experiments and sampled rocks superimposed on the multibeam bathymetry map. a, Bathymetry data and rock samples are collected from this study and the AMORE cruise[1]. Red dots with white outlines indicate the sampled basalts from this study. Dashed lines indicate the offset range where ice-station seismic signals could be identified[2]. **b-c,** Along- and across-axis profiles showing bathymetry (upper panels) and topography slope (lower panels). **d-h,** Photos of the JASMInE experiment. **d,** The icebreaker "Xuelong 2". **e,** G-gun sled being deployed. **f,** An OBS used in the JASMInE experiment. **g,** Shooting in sea ice. At times, severe sea ice conditions made the shot intermittent, and the shooting tracks deviated from the designed survey lines. **h,** Recovery of an OBS in sea ice.

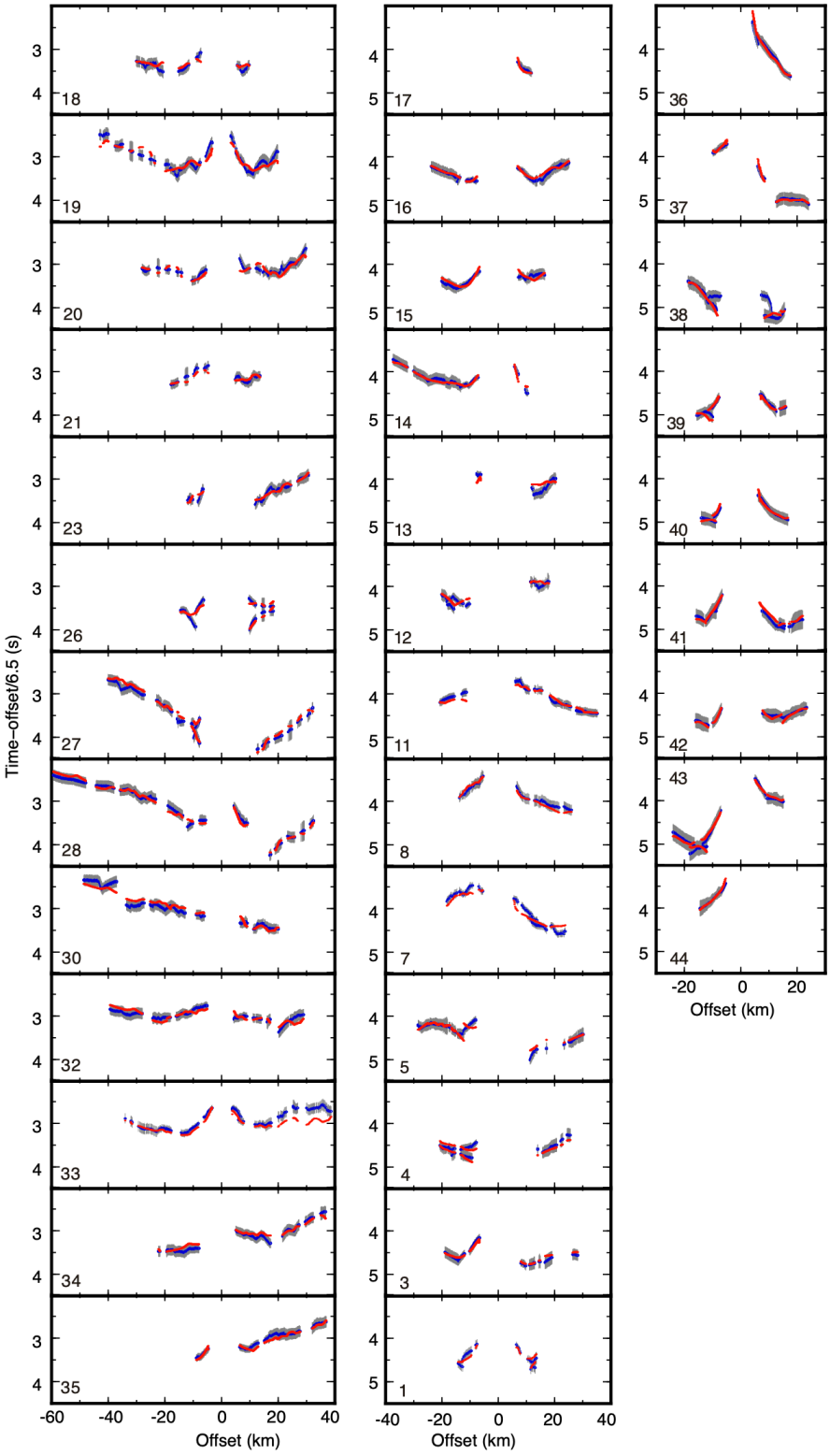

Supplementary Fig. 2 | Travel time misfit of each pick for the inversion models. Red dots show the predicted travel times. The blue dots with grey vertical bars represent the observed reflection and refraction travel times. The OBS numbers are labelled in each panel. There are relatively large misfits for refraction arrivals of OBSs 13, 38, and 33. The root-mean-square misfits of Tomo2D models along the across-axis profile and the western and the eastern sections of the along-axis profile converged at 93, 96, and 81 ms, respectively.

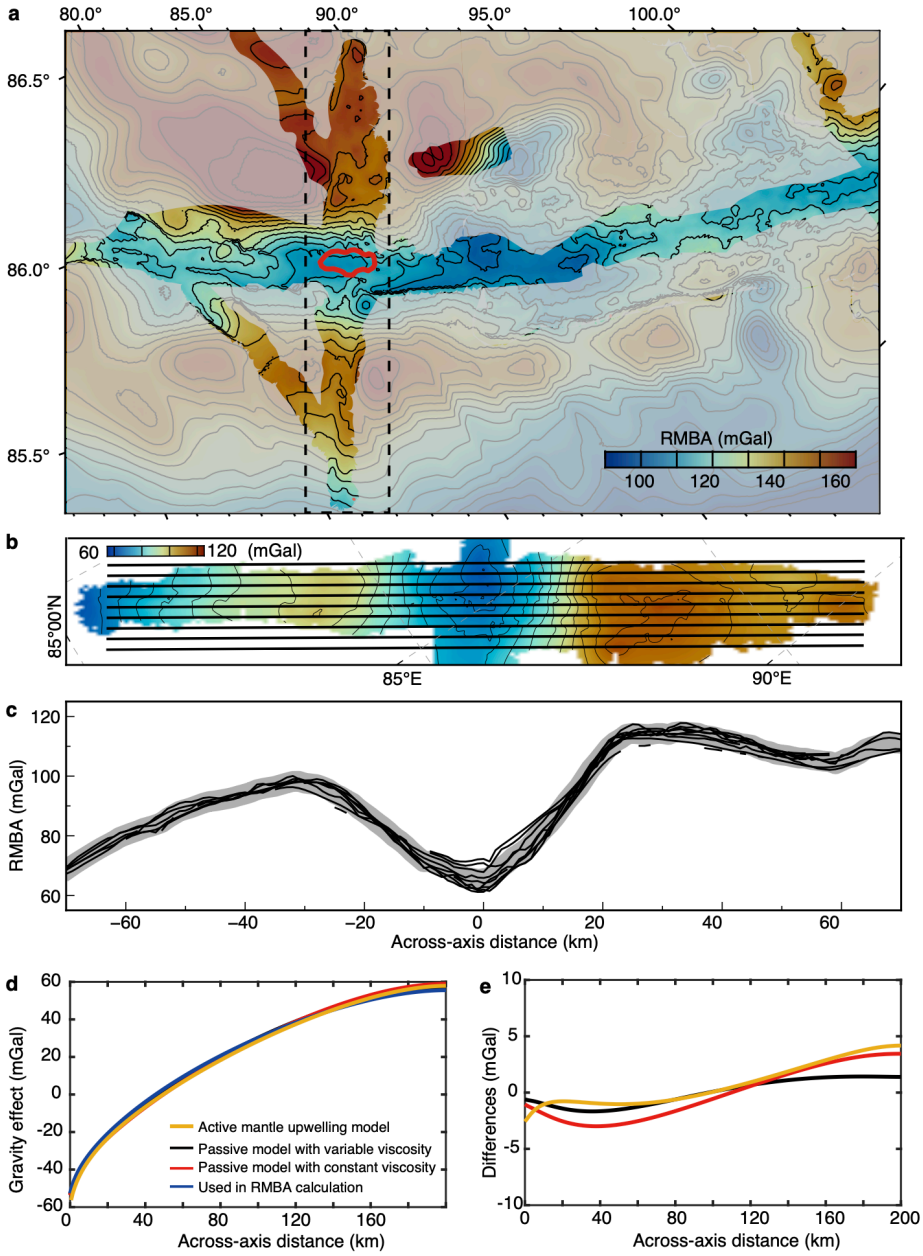

Supplementary Fig. 3 | Residual mantle Bouguer anomaly (RMBA) of the JASMInE region. a, map of RMBA. The RMBA in the areas covered by transparency were calculated from the IBCAO 4.0 and DTU 17 data. In other regions, we used multibeam bathymetry data and shipborne gravity data to calculate the RMBA. The position of 85° E volcanic centre is marked by the red line. No obvious lateral migration track of the 85° E volcanic centre is observed here. The dashed frame marks the position of panel **b**. **b,** Across-axis profiles of gravity-derived RMBA illustrate the lower RMBA is persistent in the volcanic zone covered by high-resolution data. The lower RMBA is an indication of a thick crust or a lighter mantle. **c,** RMBA profiles. The thick grey line indicates the average of the nine profiles in part **b**. Note that the effect of sediment is not considered, which may result in the low RMBA at the southern end of the profiles. **d,** Gravity effects of thermal structures for RMBA correction and in the numerical mantle upwelling models. Zero level is arbitrary. **e,** Differences in gravity effects between thermal structures for RMBA correction and the numerical active mantle upwelling (yellow), passive mantle upwelling models with constant (red) and variable (black) viscosities.

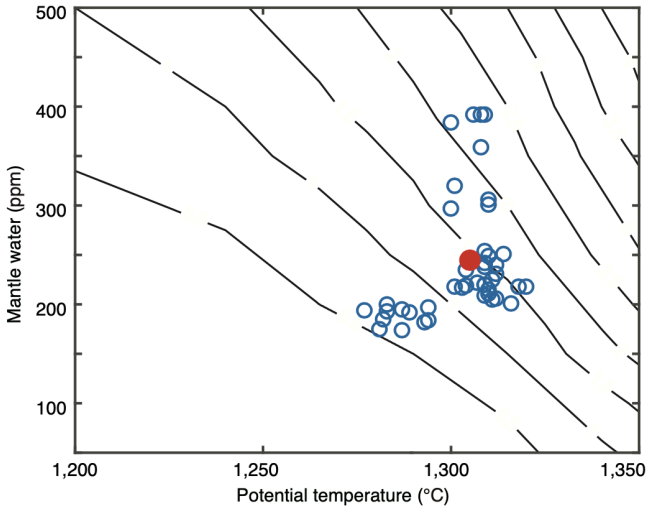

Supplementary Fig. 4 | Estimated crustal thickness with a half spreading rate of 5 mm yr^{-1}. Contours represent estimated crustal thicknesses from the model of passive mantle upwelling and wet melting[3]. The circles indicate the estimated crustal thickness with the measured T_p and water content in the JASMInE zone. The red circle shows the estimated crustal thickness with the average T_p (1,310 °C) and water content (250 ppm) of the JASMInE zone.

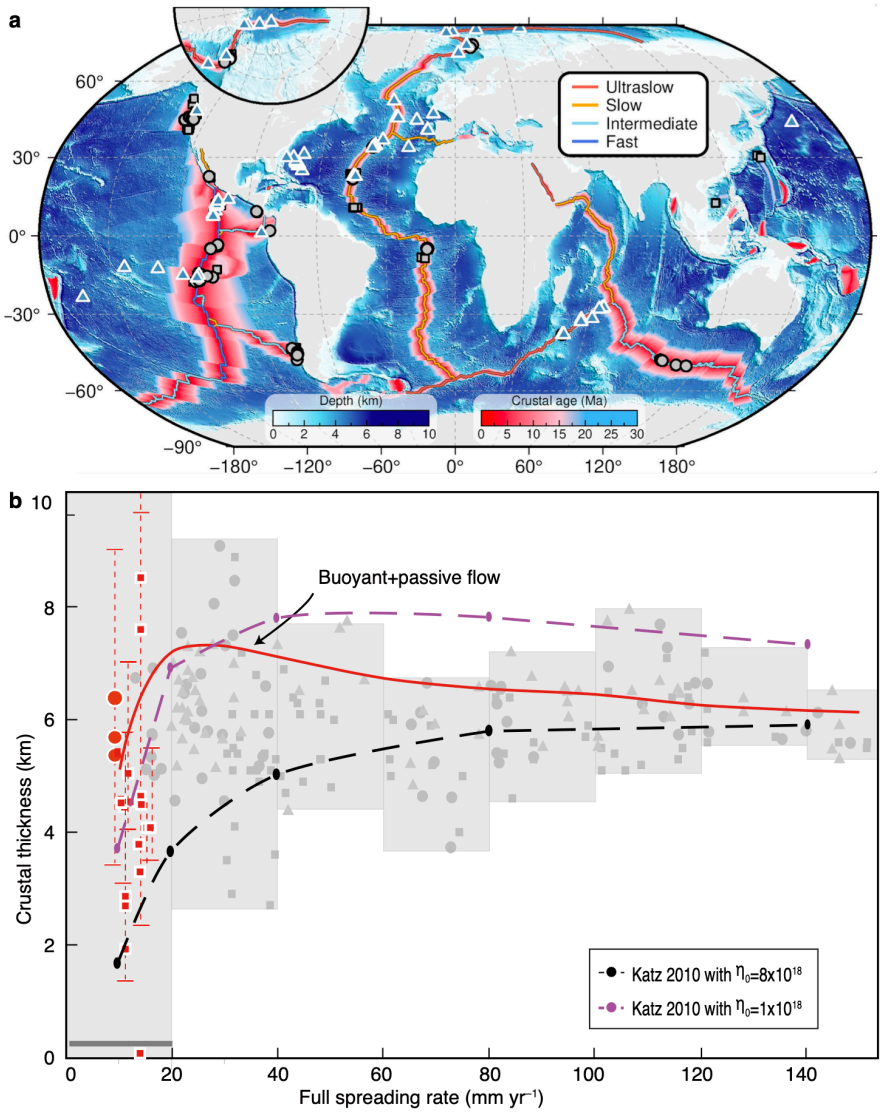

Supplementary Fig. 5 | Compilations of seismic-determined oceanic crustal thickness. a, Map of the global mid-ocean ridge system. Positions of the seismic measurement shown in b are also shown. Triangles mark the segment-average crustal thickness from ref. [4]. **b,** Values of seismic-determined crustal thickness. Dots and squares represent the crustal thickness of the data points compiled by ref. [5] and ref. [6], respectively. For comparison, results of ref. [7] with various mantle viscosity are also shown. In ref. [7], η_0 is the reference mantle viscosity at the depth just beneath the melting zone. Note that our buoyant models contain all the sources of buoyancy, including thermal, mantle depletion, and melt retention, while only melt retention-related buoyancy is considered in ref. [7].

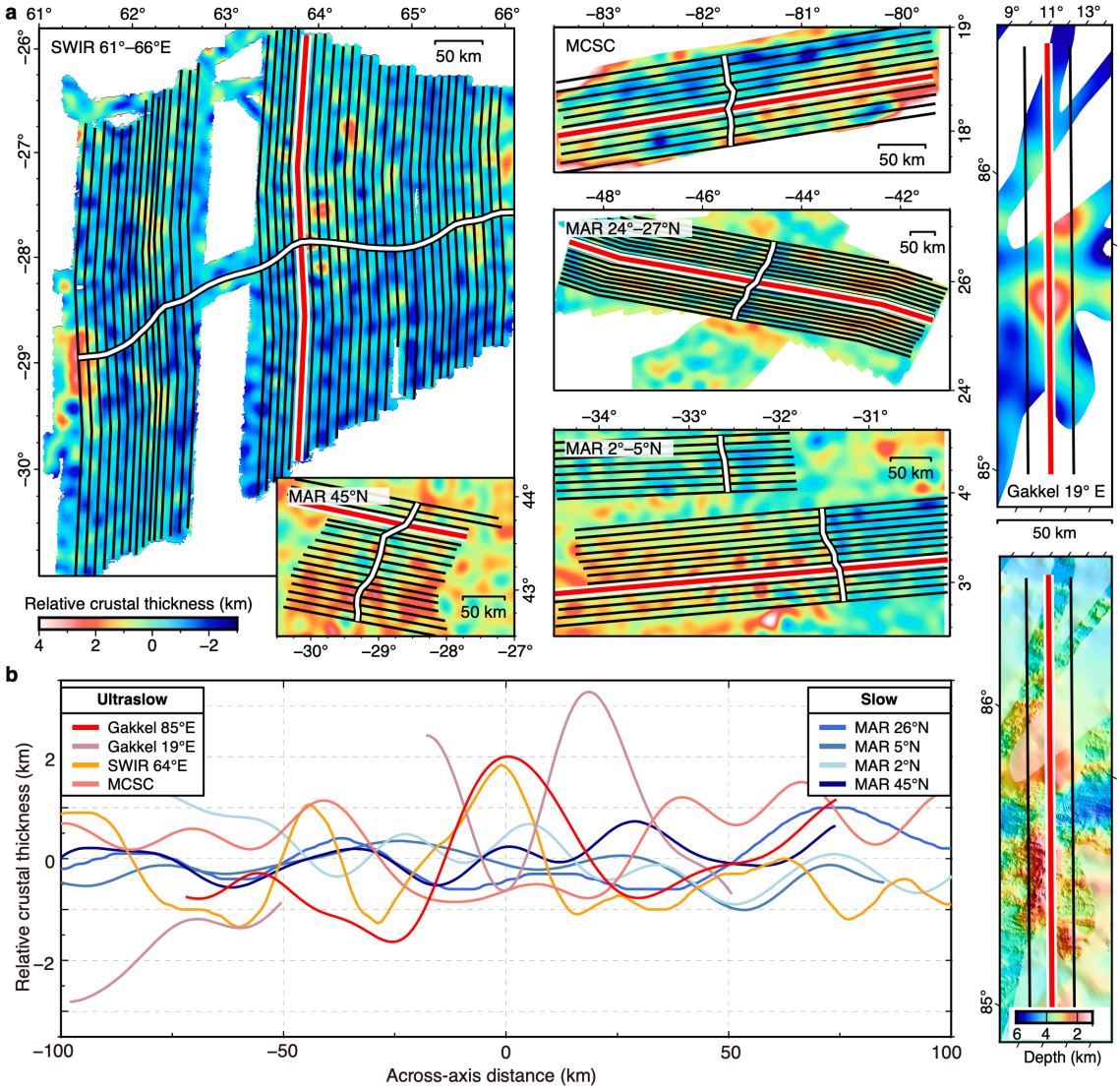

Supplementary Fig. 6 | Gravity-derived crustal thickness of selected regions of slow- and ultraslow-spreading ridges. a, maps of crustal thickness at the SWIR 61°–66° E[8], Mid-Cayman Spreading Centre (MCSC), MAR 24°–27° N[9], MAR 2°–5° N, and MAR 45° N. Except for SWIR 61°–66° E and MAR 24°–27° N, the others are calculated in this study with the constraints of shipborne bathymetry data obtained from the Global Multi-Resolution Topography Synthesis[10] and IBCAO 4.0[11], as well as satellite gravity data[12]. White lines indicate ridge axes. Red lines indicate the positions of the profile in **b**. The bathymetric map of the Gakkel at 19° E from IBCAO 4.0 is also shown. **b,** Across-axis profiles of gravity-derived crustal thickness illustrate a higher variation at ultraslow- than at slow-spreading ridges.

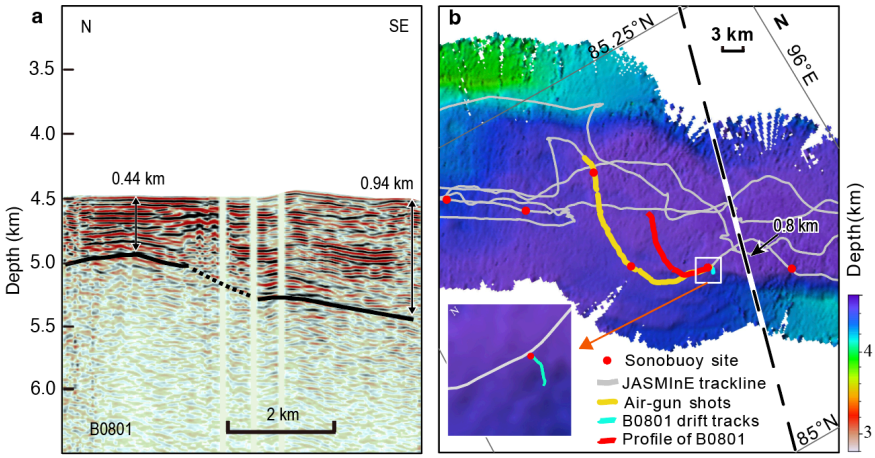

Supplementary Fig. 7 | Processed and interpreted profile of sonobuoy data (B0801 site as an example). a, Processed profile of sonobuoy B0801. The thick black line is interpreted as the sediment basement according to abrupt changes in seismic amplitudes. Seismic reflection profile (ARC 14-07)[13] near the sonobuoy B0801 for calibrating the sediment thickness. **b,** Map shows the track of sonobuoy B0801 (cyan line), location of the profile in panel **a** (red line), shooting track (yellow line), and ARC 14-07 (dashed line). At the position closest to sonobuoy B0801 track, the sediment thickness on the ARC 14-07 is approximately 0.8 km. Each sonobuoy was equipped with a GPS and transmitted real-time coordinate data to the deck.

Supplementary tables

Table 1. Sr-Nd isotopic compositions on MORB lavas from JASMInE.

Table 2. Representative major element compositions and water content of the glasses from JASMInE (In Excel format).

Table 3. Summary of identified seismic phases.

Table 4. Parameters used in numerical models.

Supplementary Table 1 | Sr-Nd isotopic compositions on MORB lavas from JASMInE.

Sample ID	Lat.(°N)	Long.(°E)	$^{87}Sr/^{86}Sr$	1σ	$^{143}Nd/^{144}Nd$	1σ	ε_{Nd}
TVG01-2	85.61	85.33	0.702723	0.000003	0.513112	0.000003	9.2
TVG01-B2	85.61	85.33	0.702593	0.000004	0.513107	0.000002	9.2
TVG01-B3	85.61	85.33	0.702585	0.000003	0.513085	0.000004	8.7
TVG02-1	85.62	85.28	0.702614	0.000003	0.513101	0.000003	9.0
TVG02-2	85.64	84.76	0.702605	0.000003	0.513111	0.000003	9.2
TVG03-1	85.63	84.78	0.702598	0.000004	0.513117	0.000003	9.3
TVG05-1	85.63	85.24	0.702610	0.000004	0.513123	0.000002	9.5
TVG07-A	85.61	85.42	0.702598	0.000003	0.513115	0.000002	9.3
TVG07-B	85.61	85.42	0.702576	0.000004	0.513097	0.000003	8.9
TVG08	84.90	99.85	0.702575	0.000003	0.513104	0.000003	9.1
TVG08-1	84.90	99.85	0.702575	0.000003	0.513111	0.000002	9.2
TVG08-2	84.90	99.85	0.702578	0.000004	0.513113	0.000002	9.3
TVG08-3	84.90	99.85	0.702584	0.000004	0.513084	0.000003	8.7
TVG08-4	84.90	99.85	0.702678	0.000003	0.513096	0.000003	8.9
BHVO-2			0.703478	0.000003			
BCR-2			0.704999	0.000003	0.512630	0.000004	
AGV-2					0.512785	0.000004	

Note: ε_{Nd} is calculated as $[(^{143}Nd/^{144}Nd)_{sample}/(^{143}Nd/^{144}Nd)_{chondrites} -1] \times 10{,}000$, where $^{143}Nd/^{144}Nd_{chondrites}=0.512638$.

Supplementary Table 2 | Representative major element compositions and water content of the glasses from JASMInE.

In Excel format.

Supplementary Table 3 | Summary of identified seismic phases*.

Profiles	Sites	PW	P2	P3	PmP	Pn
Across-axis profile	OBS 18	√	√	√		√
	OBS 19	√	√	√		√
	OBS 20	√	√	√		
	OBS 21	√	√	√		
	OBS 23	√	√	√		√
	OBS 26	√	√	√	√	
	OBS 27	√	√		√	√
	OBS 28	√	√	√	√	√
	OBS 30	√	√	√		√
	OBS 32	√	√	√	√	√
	OBS 33	√	√	√		√
	OBS 34	√	√	√		√
	OBS 35	√	√	√		√
Western section of the along-axis profile	OBS 17	√	√			
	OBS 16	√	√	√		√
	OBS 15	√	√	√		√
	OBS 14	√	√			√
	OBS 13	√	√	√		
	OBS 12	√		√	√	√
	OBS 11	√	√	√		
	OBS 8	√	√	√		
	OBS 7	√	√	√		
	OBS 5	√	√	√	√	√
	OBS 4	√	√	√	√	√
	OBS 3	√	√	√	√	√
	OBS 1	√	√		√	√
Eastern section of the along-axis profile	OBS 36	√	√	√		
	OBS 37	√	√		√	
	OBS 38	√	√	√	√	√
	OBS 39	√	√		√	
	OBS 40	√	√		√	
	OBS 41	√	√		√	√
	OBS 42	√	√		√	
	OBS 43	√	√		√	√
	OBS 44	√	√			

* "√" represent the seismic phase can be identified in the OBS.

Supplementary Table 4 | Parameters used in numerical models.

Variable	Meaning	Value	Units
g	Acceleration of gravity	10	m s^{-2}
α	Thermal expansivity	$3x10^{-5}$	$°C^{-1}$
ρ_0	Reference density of unmelted mantle	3,300	kg m^{-3}
ρ_ζ	Density reduction due to total depletion	100	kg m^{-3}
ρ_ϕ	Density reduction due to melt retention	300	kg m^{-3}
T_0	Reference mantle temperature	1,350	°C
η_0	Reference viscosity of unmelted mantle at the model bottom	[$5x10^{18}$–10^{20}]	Pa s
E	Activation energy	250	kJ mol^{-1}
V	Activation volume	$4x10^{-6}$	m^3 mol^{-1}
R	Universal gas constant	8.314	J mol^{-1} K^{-1}
U_0	Half spreading rate	[5–70]	mm yr^{-1}

References

1. Michael, P. J. *et al.* Magmatic and amagmatic seafloor generation at the ultraslow-spreading Gakkel ridge, Arctic Ocean. *Nature* **423**, 956–961 (2003).

2. Jokat, W. & Schmidt-Aursch, M. C. Geophysical characteristics of the ultraslow spreading Gakkel Ridge, Arctic Ocean. *Geophys J Int* **168**, 983–998 (2007).

3. Robinson, C. J., Bickle, M. J., Minshull, T. A., White, R. S. & Nichols, A. R. L. Low degree melting under the Southwest Indian Ridge: the roles of mantle temperature, conductive cooling and wet melting. *Earth Planet Sci Lett* **188**, 383–398 (2001).

4. White, R. S., Minshull, T. A., Bickle, M. J. & Robinson, C. J. Melt generation at very slow-spreading oceanic ridges: constraints from geochemical and geophysical data. *J Petrol* **42**, 1171–1196 (2001).

5. Christeson, G. L., Goff, J. A. & Reece, R. S. Synthesis of oceanic crustal structure from two-dimensional seismic profiles. *Rev Geophys* **57**, 504–529 (2019).

6. Harding, J. L. *et al.* Magmatic-tectonic conditions for hydrothermal venting on an ultraslow-spread oceanic core complex. *Geology* **45**, 839–842 (2017).

7. Katz, R. F. Porosity-driven convection and asymmetry beneath mid-ocean ridges. *Geochem Geophys Geosyst* **11**, Q0AC07 (2010).

8. Cannat, M. *et al.* Modes of seafloor generation at a melt-poor ultraslow-spreading ridge. *Geology* **34**, 605–608 (2006).

9. Wang, T., Tucholke, B. E. & Lin, J. Spatial and temporal variations in crustal production at the Mid-Atlantic Ridge, 25°N–27°30′N and 0–27 Ma. *J Geophys Res* **120**, 2119–2142 (2015).

10. Ryan, W. B. F. *et al.* Global Multi-Resolution Topography synthesis. *Geochem Geophys Geosyst* **10**, Q03014 (2009).

11. Jakobsson, M. *et al.* The international bathymetric chart of the Arctic Ocean version 4.0. *Sci Data* **7**, 176 (2020).

12. Andersen, O. B., Knudsen, P., Kenyon, S., Holmes, S. & Factor, J. K. Evaluation of the global altimetric marine gravity field DTU15: using marine gravity and GOCE satellite gravity. *Iag Symp* 77–81 (2019) doi:10.1007/1345_2018_52.

13. Nikishin, A. M., Gaina, C., Petrov, E. I., Malyshev, N. A. & Freiman, S. I. Eurasia Basin and Gakkel Ridge, Arctic Ocean: crustal asymmetry, ultra-slow spreading and continental rifting revealed by new seismic data. *Tectonophy* **746**, 64–82 (2018).